Transient characteristics of flow boiling in large micro-channel heat exchangers

Seunghyun Lee, Issam Mudawar *

Boiling and Two-Phase Flow Laboratory (PU-BTPFL), School of Mechanical Engineering, Purdue University, 585 Purdue Mall, West Lafayette, IN 47907, USA

ABSTRACT

This study investigates both time-averaged and transient characteristics of large area micro-channel evaporators incorporated into an R-134a vapor compression loop that simulates thermal control for future space vehicles. The loop contains two separate micro-channel evaporators, one to simulate heat acquisition from the spacecraft crew and the other from the avionics. Both evaporators feature parallel 1×1-mm^2 micro-channels, with the smaller crew evaporator yielding relatively low qualities, and the larger avionics evaporator both low and high qualities. Heat transfer measurement and high speed video are used to investigate variations of heat transfer coefficient with quality for different mass velocities and heat fluxes, as well as transient fluid flow and heat transfer behavior. Relatively low qualities in the crew evaporator are dominated by slug flow and the nucleate boiling mechanism. On the other hand, the avionics evaporator produces different flow regimes and heat transfer mechanisms depending on quality range, with low qualities associated with slug flow and dominated by nucleate boiling, and high qualities by annular flow and convective boiling. Further increases in quality trigger incipient dryout of the annular film and transition to mist flow. An important transient phenomenon that influences both fluid flow and heat transfer is a liquid wave composed of remnants of liquid slugs from the slug flow regime. The liquid wave serves to replenish dry wall patches in the slug flow regime and to a lesser extent the annular regime. Two-phase flow in the two evaporators shows clear signs of parallel-channel instability.

© 2016 Elsevier Ltd. All rights reserved.

1. Introduction

1.1. Implementation of vapor compression loop in spacecraft Thermal Control Systems (TCSs)

Managing heat dissipation in future manned space missions is complicated by anticipated increases in power consumption and waste heat dissipation [1]. The heat dissipation onboard spacecraft is managed with the aid of a Thermal Control System (TCS), which is tasked with heat acquisition from crew and avionics, heat transport to a condenser/radiator, and heat rejection from the radiator. And while past spacecraft have relied on single-phase liquid TCS, there is now serious interest in using two-phase TCS to capitalize on weight reductions made possible by greatly improved heat transfer performance realized with flow boiling and condensation.

Aside from the need to manage greatly increased amounts of heat, future spacecraft are expected to tackle different types of missions (e.g., missions to near Earth objects, Lunar surface,

Martian surface, and deep space), with vastly different gravitational as well as temperature environments [2]. The latter can be classified into 'cold' environments, associated with heat sink temperatures that are lower than that of the TCS working fluid, and 'warm' environments, where the heat sink temperature exceeds that of the working fluid. While cold environments allow heat rejection from the TCS condenser/radiator using a pumped two-phase loop, warm environments necessitate the use of a vapor compression heat pump to reject the heat. Two specific mission stages that require vapor compression are Low Lunar Orbit (LLO) and Low Mars Orbit (LMO), with heat sink temperatures as high as 17 and 22 °C, respectively, both exceeding the lowest coolant temperature in the TCS evaporators of about 5 °C [2].

To tackle both cold and warm environments, Singh and Hasan [3] proposed the concept of a reconfigurable TCS that could operate as a pumped two-phase loop in cold environments, or a vapor compression loop in warm environments. Lee et al. [2] investigated the thermodynamic performance of this Hybrid Thermal Control System (H-TCS) for different space missions and identified R134a as optimum working fluid. The present study concerns the heat pump configuration of a H-TCS. Addressed in this study are dominant

---

* Corresponding author. Fax: +1 (765) 494 0539.
E-mail address: mudawar@ecn.purdue.edu (I. Mudawar).
URL: http://engineering.purdue.edu/BTPFL (I. Mudawar).

Nomenclature

A_{base}	total base area of heat sink
C_n	complex Fourier coefficient
C_n^*	complex conjugate Fourier coefficient
D_h	hydraulic diameter
F	frequency
$\hat{f}$	discrete Fourier transform
$\hat{f}^*$	complex conjugate of discrete Fourier transform
f_k	complex form of Fourier series
G	mass velocity
h	enthalpy
H_{ch}	micro-channel height
h_{fg}	latent heat of vaporization
H_{tc}	distance between thermocouple and bottom of micro-channel
h_{tp}	local two-phase heat transfer coefficient
j	superficial velocity
k	thermal conductivity
L	length of micro-channel
m	fin parameter
$\dot{m}$	total mass flow rate of heat sink
N	total number of measurement points
P	pressure
P	average power spectrum
q''	heat flux based on total base area of heat sink
Re	Reynolds number
Su	Suratman number
T	temperature
ΔT_{sat}	wall superheat, $\Delta T_{sat} = T_{w,b} - T_{sat}$
u	fluid velocity
$\bar{u}$	average fluid velocity
W_{ch}	micro-channel channel width
We^*	modified Weber number
W_w	half-width of copper sidewall separating micro-channels

x_e	thermodynamic equilibrium quality
x_k	sampling point in time
X_{tt}	turbulent–turbulent Lockhart–Martinelli parameter
z	axial coordinate

Greek symbols

δ	film thickness
η	fin efficiency
μ	dynamic viscosity
v	kinematic viscosity
ρ	density
σ	surface tension

Subscripts

air	air
$avionics$	avionics HX
b	bottom of micro-channel
ch	micro-channel
cor	corrected
$crew$	crew HX
f	liquid
g	vapor
in	micro-channel inlet
lf	liquid film
Nyq	Nyquist frequency
ONB	onset of nucleate boiling
out	micro-channel outlet
s	solid (copper); sampling
sat	saturation
tc	thermocouple
tp	two-phase flow
w	micro-channel wall

flow patterns and heat transfer mechanisms associated with flow boiling in H-TCS evaporators.

Several schemes are available to dissipate heat by boiling [4], and while these schemes offer competing advantages and disadvantages, micro-channel boiling is ideally suited for spacecraft applications because of such factors as ability to achieve very high heat transfer coefficients, greatly decrease system weight and volume, reduce fluid inventory, tackle heat input from multiple heat sources, and minimize impact of reduced gravity on flow boiling compared to macro channels.

1.2. Nucleate boiling in micro-channels

Two mechanisms commonly associated with flow boiling in micro-channels are *nucleate boiling* and *convective boiling* [5,6]. Nucleate boiling is encountered in low quality bubbly and slug flow regimes in the upstream region of the channel and dominated by bubble nucleation. On the other hand, convective boiling is associated with downstream annular flow, dominated by heat transfer to the annular film, coupled with evaporation along the film's interface. Much of the difficulty predicting the magnitude of local heat transfer coefficient in a micro-channel stems from the inability to determine which of the two mechanisms is most prevalent, and the axial location associated with transition from nucleate boiling to convective boiling.

A key mechanism that governs the transition from nucleate to convective boiling is *suppression of nucleate boiling*. According to

[7], nucleation in saturated flow boiling will commence on a wall cavity when the wall heat flux exceeds the heat flux corresponding to the onset of nucleate boiling (ONB), given by

$$q''_{ONB} = \frac{k_f h_{fg} \rho_g}{8\sigma T_{sat}} \Delta T_{sat}^2,\qquad(1)$$

where ΔT_{sat} is the wall superheat. For saturated flow boiling, $q'' = h\Delta T_{sat}$, where h is the heat transfer coefficient, which reduces Eq. (1) to

$$q''_{ONB} = \frac{8\sigma T_{sat} h^2}{k_f h_{fg} \rho_g}.\qquad(2)$$

For a uniformly heated micro-channel, nucleation is abundant in the upstream low quality region associated with mostly bubbly and slug flow regimes as discussed above. However, as quality increases downstream, annular flow is gradually established, where the heat is transferred mostly across the annular film and to a much lesser extent by nucleation along the wall. Gradual increases in quality and vapor shear cause simultaneous thinning and acceleration of the annular film, which enhances the heat transfer coefficient. Eq. (2) proves this increase in h in the annular region decreases the ability to sustain nucleation downstream; this is the basis for the aforementioned suppression phenomenon.

Thermodynamic equilibrium quality, x_e, is one of the key parameters investigators rely upon when identifying dominant heat transfer mechanisms in micro-channels. The magnitude of

x_e for a given working fluid is dictated by both heat flux and mass velocity. Kew and Cornwell [8] examined the dependence of nucleate boiling on tube diameter for R141b in horizontal 500-mm long tubes with diameters ranging from of 1.39 to 3.69 mm. They showed that heat transfer performance is strongly influenced by bubble confinement effects for smaller diameters. A stronger influence of heat flux on heat transfer coefficient was realized for larger diameters, and the transition from bubbly and/or slug flow to annular flow occurred earlier with smaller diameters. Additionally, nucleate boiling suppression quality increased with increasing tube diameter because of the diminishing effects of bubble confinement. Lin et al. [9] investigated the influence of heat flux on heat transfer coefficient trends for R141b in a vertical 1-mm diameter, 500-mm long tube over a mass velocity range of 300–2000 kg/m^2 s and heat fluxes from 18 to 72 kW/m^2. They showed that the nucleate boiling dominant region, where the heat transfer coefficient increases with increasing heat flux and decreasing quality, can extend up to x_e = 0.5, and the quality corresponding to suppression of nucleate boiling is a function of heat flux. In and Jeong [10] investigated flow boiling of R134a in a 0.19-mm diameter, 31-mm long tube with a heated length of 20.6 mm. Nucleate boiling was dominant for x_e < 0.6, corresponding to heat fluxes from 10 to 20 kW/m^2 and mass velocities of 392–470 kg/m^2 s.

Similar flow boiling studies were performed with heat sinks containing multiple micro-channels. Using a 44.8-mm long copper heat sink containing 21 of 231×713-μm^2 rectangular micro-channels, Qu and Mudawar [11] showed that the relatively high surface tension of water results in larger bubble departure diameters, promoting rapid transition from bubbly to annular flow close to the inlet. Lee and Mudawar [12] examined flow boiling of R134a in a 25.3×25.3-mm^2 heat sink containing 53 of 231×713-μm^2 micro-channels and identified dominant heat transfer mechanisms corresponding to different quality ranges. The nucleate boiling dominant regime, where the heat transfer coefficient is highly influenced by heat flux, was achieved up to x_e = 0.55.

1.3. Convective boiling in micro-channels

Convective boiling heat transfer is encountered in the annular flow regime and comprised of heat transfer between the wall and the annular liquid film. Lee and Lee [13] used the film's Reynolds number, based on thickness, δ, and mean velocity, u_{lf}, of the liquid film, $Re_{lf} = (4u_{lf}\delta)/v_f$, to distinguish two limiting heat transfer mechanisms: laminar film conduction for Re_{lf} < 200, and turbulent film convection for Re_{lf} > 200. Laminar film conduction is achieved when the film thickness is very small. Here, the magnitude of two-phase heat transfer coefficient, h_{tp}, is dictated entirely by conduction across the liquid film, $h_{tp} = k_f/\delta$. The heat transfer coefficient increases in the flow direction as the film becomes gradually thinner due to both evaporation and increased vapor shear resulting from the axially increasing quality. Turbulent film convection occurs with thicker films and is dominated mostly by turbulent mixing.

Overall, convective boiling is dominant mostly in low flux situations. Saitoh et al. [14] investigated flow boiling of R134a in tubes with diameters and lengths ranging from 0.51 to 3.1 mm, and 550 to 3255 mm, respectively, with mass velocities of 150–450 kg/m^2 s and heat fluxes ranging from 5 to 39 kW/m^2. The increase in heat transfer coefficient with increasing mass velocity was stronger for larger tube diameters because of more effective convective boiling, which may be the result of stronger turbulence mixing in the liquid film. The heat flux effect for low qualities was strong irrespective of tube diameter. Tibiriçá and Ribatski [15] measured the heat transfer coefficient for R134a in a 2.3-mm diameter,

464-mm long tube, with mass velocities ranging from 100 to 600 kg/m^2 s and a heat flux of 15 kW/m^2, and showed that convective heat transfer was dominant over the entire tube length. Ducoulombier et al. [16] investigated flow boiling of CO_2 in a 0.529-mm diameter, 191-mm long tube with mass velocities in the range of 200 to 1200 kg/m^2 s and a heat flux of 10 kW/m^2, and demonstrated the dominance of convective boiling over nucleate boiling for x_e > 0.4, evidenced by strong dependence of the heat transfer coefficient on vapor quality and mass velocity.

1.4. Flow oscillations and instabilities due to flow boiling in micro-channels

Recent studies have revealed that flow boiling in micro-channels is associated with specific types of flow oscillations and instabilities, which can be categorized relative to period of oscillation. *Long periods* have been measured in experiments involving flow resulting from pressure difference between two reservoirs. Wu and Cheng [17] measured pressure and temperature fluctuation periods of 31 and 141 s for flow boiling of water in 33-mm long micro-channels with 158.8 and 82.8 μm hydraulic diameters, respectively. Huh et al. [18] also used two reservoirs and dual operation syringe pump to deliver fluid to the test section, and measured fluctuation periods of 100–200 s for flow boiling of water in a 40-mm long micro-channel with a hydraulic diameter of 103.5 μm.

Both *intermediate periods* and *short periods* of oscillation have been measured during flow boiling in heat sinks containing parallel micro-channels. Using the 44.8-mm long heat sink containing 21 of 231×713-μm^2 rectangular micro-channels as discussed above, Qu and Mudawar [19] encountered two types of fluctuations during water flow boiling. Identified as *pressure-drop oscillation*, the first type consisted of large amplitude (about 0.3 bar) fluctuations with an *intermediate period* of 10 s, and was manifest by axial boundaries between flow regimes in the parallel micro-channels oscillating in unison. This type of instability was virtually eliminated by isolating compressibility effects in the heat sink from those in the upstream flow loop using a control valve situated immediately upstream of the heat sink. However, after effectively eliminating the large amplitude pressure-drop oscillation with the aid of the control valve, Qu and Mudawar encountered a different type of fluctuations, which took the form of *parallel-channel instability* associated with *density-wave oscillations* in individual channels. Both pressure drop and flow rate became chaotic as slight inlet pressure variations among micro-channels caused density waves to travel through different micro-channels at slightly different times. This instability was characterized by relatively small amplitude (0.15 bar) pressure drop fluctuations with a *short period* of 2 s. Here, the axial boundaries between flow regimes in the parallel micro-channels oscillated in a random manner. And, unlike the pressure-drop oscillation, the parallel-channel instability could not be eliminated by upstream throttling.

In the flow boiling experiments of R134a in a 3.1-mm diameter and 3235-mm long tube, Saitoh et al. [14] showed that the flow fluctuations occur when inlet quality is lower than 0.13, at which the flow pattern changes from slug to wavy-annular. The heat transfer coefficient rapidly decreased once the flow fluctuations commenced. Furthermore, dryout incipience was attributed to the flow fluctuations that were initiated by this flow regime transition.

Density-wave oscillation is the most common type of flow boiling instability, and is caused by feedback between flow rate, vapor generation, and pressure drop [20]. Ding et al. [21] showed that density-wave oscillations for R-11 in a 10.9-mm diameter and

1060-mm long steel tube are associated with relatively short periods ranging from 0.3 to 1 s. Studies have shown that density-wave oscillation period depends on the time required for the density wave to travel between the two ends of the flow channel [22,23].

Chang and Pan noted that the magnitude of pressure drop oscillation is related to the appearance of reversed flow, and presented a flow stability map using dimensionless inlet subcooling number and phase change number [24].

1.5. Objectives of study

The present study concerns the transient two-phase flow and heat transfer characteristics of large area micro-channel evaporators incorporated into a vapor compression loop. The transient behavior is investigated in relation to several inter-related flow and heat transfer regimes, and associated mechanisms, including

1. Dominant flow regimes, mostly bubbly/slug versus annular.
2. Dominant heat transfer regimes, mostly nucleate boiling versus convective boiling.
3. Transitions between heat transfer regimes, including intermittent dryout in bubbly and slug flow, dryout incipience in annular flow, and dryout completion into mist flow [25].
4. Different possible types of instability, including pressure drop oscillation and parallel channel instability.
5. Important transient mechanisms, including propagation of a liquid wave along the channel.

2. Experimental methods

2.1. Vapor compression facility

Fig. 1(a) shows the layout of the R134a vapor compression loop constructed for this study. The central components of the loop are two micro-channel heat exchangers, crew HX and avionics HX, that serve as evaporators for the loop, and are sized to tackle the total heat rates associated with the crew and avionics, respectively, in a H-TCS system. The loop is comprised of a Copeland scroll compressor that is fitted upstream with a suction accumulator, which both ensures only vapor flows into the compressor and helps regulate the refrigerant flow, and downstream by an oil separator. The compressed vapor is passed to a Trenton air-cooled condenser, where it is converted to subcooled liquid, followed by a liquid reservoir and a turbine flow meter. The subcooled liquid is then throttled into a two-phase mixture using two control valves connected in series, reducing pressure by isenthalpic expansion to the desired crew HX's inlet value. Additional details concerning the vapor compression loop and its components and instrumentation are available in a previous study by the authors [25].

2.2. Crew and avionics HXs

Fig. 1(b) shows a photo of the crew and avionics HXs. Each HX contains an oxygen-free copper plate – heat sink – into which parallel 1×1-mm^2 micro-channels are machined. The heat sinks in the crew HX and avionics HX measure 152.4 mm long by
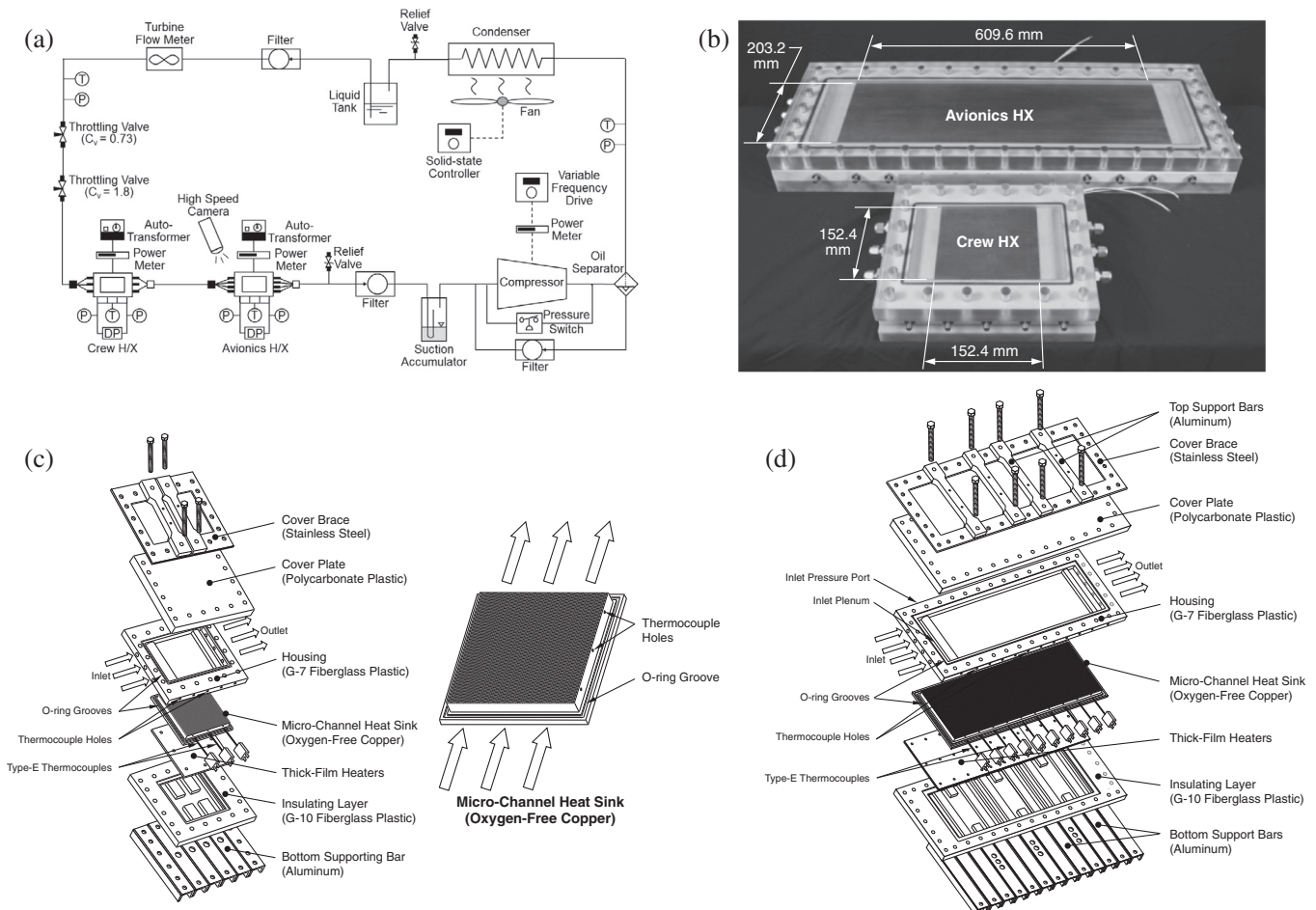
Fig. 1. (a) Schematic diagram of vapor compression loop. (b) Photo of avionics HX and crew HX. (c) Exploded view of crew HX. (d) Exploded view of avionics HX.

Table 1
Crew and avionics micro-channel heat sink dimensions.

	Length [mm]	Width [mm]	Number of channels	Thermocouple axial locations [mm]
Crew HX	152.4	152.4	75	22.9, 76.2, 129.5
Avionics HX	609.6	203.2	100	44.2, 102.1, 160.0, 217.9, 275.8, 333.8, 391.7, 434.3, 507.5, 565.4

152.4 mm wide, and 609.6 mm long by 203.2 mm wide, respectively, with the former containing 75 micro-channels and the latter 100 micro-channels.

Fig. 1(c) and (d) show detailed exploded views of the crew and avionics HXs, respectively. The heat sinks are heated uniformly along their underside using Watlow thick film heaters. The copper heat sink temperatures are measured at several axial locations detailed in Table 1 using Type-E thermocouples. Each thermocouple is inserted along a stainless steel sheath, with the junction positioned along the centerline of the heat sink. The micro-channels in each HX are closed atop with a transparent cover plate made from polycarbonate plastic (Lexan) to facilitate photographic access to the two-phase flow in the micro-channels using a Photron-Ultima APX high-speed video camera. The heat sink is mounted into an insulating G-7 fiberglass plastic housing, which features inlet and outlet plenums intended to enhance uniformity in flow distribution among micro-channels, and where the fluid's pressure and temperature are measured. Another layer of insulating G-10 fiberglass plastic is used to minimize heat loss from the perimeter and underside of the thick-film heater. The crew and avionics HXs are reinforced with metal braces to ensure tight assembly and minimize buckling of intermediate layers.

2.3. Operating conditions

As indicated above, the throttling valves are responsible for decreasing liquid pressure to the desired crew HX's inlet pressure, causing the liquid to flash into a two-phase mixture. Assuming isenthalpic pressure drop, the fluid's enthalpy at the inlet to the crew HX is equal to the enthalpy determined from pressure and temperature measurements of liquid upstream of the throttling valves. Using this enthalpy value, h, the vapor quality at the inlet to the crew HX is determined as $x_{e,in} = (h - h_f)/h_{fg}$, where h_f and h_{fg} are saturated values based on the pressure measured at the crew HX's inlet. The crew and avionics HX's outlet qualities are determined by applying an energy balance to the entire HX, $x_{e,out} = x_{e,in} + (q''A_{base})/\dot{m}h_{fg}$, where q'' is the heat flux based on the heat sink's bottom area, A_{base}, and $\dot{m}$ the total flow rate of R134a.

Detailed operating conditions of the study are provided in Table 2, and measurement uncertainty information in [25].

2.4. Determination of heat transfer coefficient

Fig. 2(a) shows a photo of the heat sink surface with details of a single micro-channel. A unit cell comprised of a single micro-channel, two half copper sidewalls, and surrounding materials is shown in Fig. 2(b). The unit cell is used to determine the micro-channel's bottom wall temperature, $T_{w,b}$, assuming one dimensional heat diffusion, $T_{w,b} = T_{tc} - (q''H_{tc})/k_s$, where T_{tc}, q'', H_{tc}, and k_s are, respectively, the temperature measured by the heat sink thermocouple, heat flux based on the heat sink's bottom surface area, distance between the thermocouple junction and micro-channel's bottom wall, and thermal conductivity of copper. The heat transfer coefficient, h_{tp}, is calculated by applying an energy balance to the unit cell in Fig. 2(b), with the sidewalls treated as fins with fin efficiency η,

$$h_{tp} = \frac{q''(W_{ch} + 2\,W_w)}{(T_{w,b} - T_{f,sat})(W_{ch} + 2\,\eta\,H_{ch})}. \tag{3}$$

Assuming fins with adiabatic tips [26], the fin efficiency is given by $\eta = \tanh(mH_{ch})/(mH_{ch})$, where m is the fin parameter, given by $m = \sqrt{h_{tp}/(k_s W_w)}$. Dimensions of the micro-channel heat sink unit cell in both the crew HX and avionics HX are: W_{ch} = 1.0 mm, H_{ch} = 1.0 mm, W_w = 0.5 mm, and H_{tc} = 4.08 mm.

3. Experimental results

3.1. Intermittent dryout, dryout incipience and dryout completion

Because of their relative locations in the flow loop, with the crew HX situated upstream of the avionics HX, and larger size and higher power input of the latter, relatively low exit vapor qualities, $x_{e,out}$ = 0.1191–0.5298, are achieved at the exit of the crew HX, compared to both low and high qualities, $x_{e,out}$ = 0.4071–1.5677, at the exit of the avionics HX. The low quality values in the avionics

Table 2
Operating conditions for crew HX and avionics HX.

| $q''_{avionics}$ [W/m²]	$G_{avionics}$ [kg/m² s]	$x_{e,in}$	$x_{e,out}$	Number of h_{tp} data points (1000 total)
Avionics HX				
8072.9	152.90–225.97	0.1850–0.2377	0.4071–0.5586	50
12,109.4	155.27–266.84	0.1641–0.2324	0.4496–0.6995	70
16,145.9	154.66–286.18	0.1475–0.2367	0.5060–0.8599	80
20,182.3	154.45–322.53	0.1389–0.2269	0.5464–1.2233	100
24,218.8	153.70–359.93	0.1108–0.2332	0.5533–1.4369	120
28,255.3	152.83–361.70	0.1052–0.2274	0.6211–1.5677	120
32,291.7	172.31–381.24	0.0868–0.2121	0.6546–1.5369	120
36,328.2	193.07–398.55	0.0891–0.1892	0.6941–1.4988	120
40,364.7	232.60–416.25	0.0852–0.1654	0.7450–1.3366	110
44,401.1	249.63–434.31	0.0703–0.1511	0.7671–1.3598	110
q''_{crew} [W/m²]	G_{crew} [kg/m² s]	$x_{e,in}$	$x_{e,out}$	Number of h_{tp} data points (144 total)
Crew HX				
8072.9	229.33–529.63	0.0729–0.1974	0.1191–0.2715	24
16,145.9	230.59–527.18	0.0765–0.1951	0.1528–0.3250	24
24,218.8	229.30–528.50	0.0700–0.1922	0.1744–0.3825	24
32,291.7	230.94–532.27	0.0515–0.1785	0.1823–0.4253	24
40,364.7	229.00–526.96	0.0626–0.1787	0.2278–0.4883	24
48,437.6	233.34–530.72	0.0535–0.1627	0.2448–0.5298	24
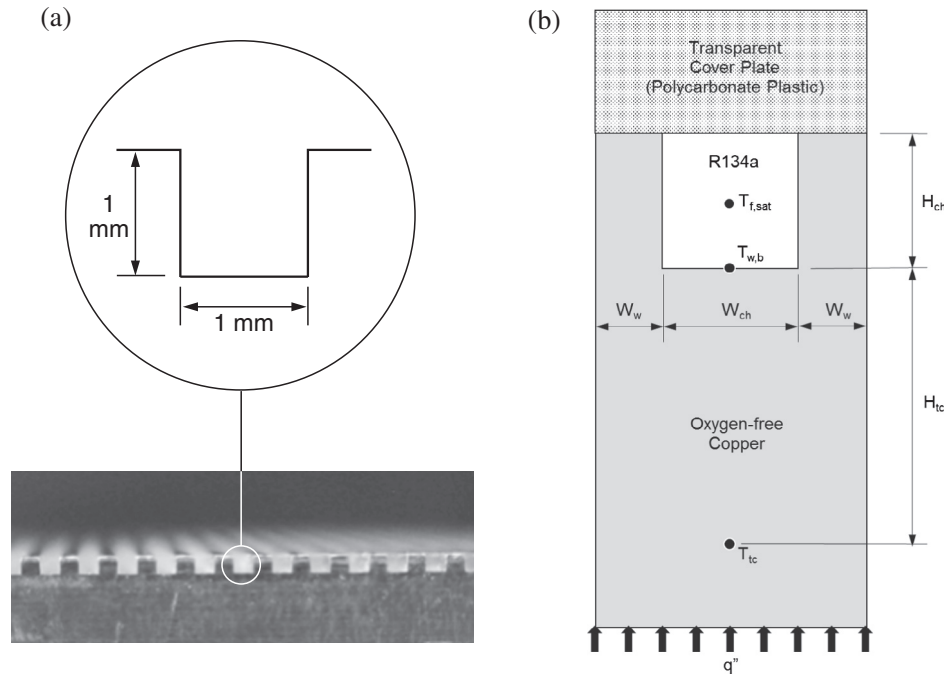
Fig. 2. (a) Cross-section of micro-channel machined into copper heat sink. (b) Micro-channel unit cell.

HX are achieved by setting power input to the upstream crew HX to zero.

In a recent paper [25], the authors of the present study investigated the variation of the two-phase heat transfer coefficient, h_{tp}, with thermodynamic equilibrium quality, x_e, along the avionics HX, and summarized the corresponding dominant heat transfer mechanisms. This variation is shown in Fig. 3(a) for $q''_{avionics}$ = 44,401.1 W/m^2 and $G_{avionics}$ = 340.23 kg/m^2 s, with the corresponding dominant heat transfer mechanisms depicted schematically in Fig. 3(b). Fig. 3(a) shows h_{tp} increases slightly in the upstream bubbly flow region, decreases slightly in the ensuing slug flow region by bubble confinement, then increases again in the annular region, before decreasing drastically towards the downstream mist flow region. Fig. 3(b) shows three dominant heat transfer mechanisms. Shown in schematic (i) in Fig. 3(b), flow boiling in the low quality region (x_e < 0.36, X_{tt} > 0.31, We^* < 9.4) is comprised of bubbly and slug flow, where heat transfer is dominated by nucleate boiling corresponding to high h_{tp} values. Nucleate boiling heat transfer in the slug flow regime is the result of both bubble nucleation in liquid slugs and evaporation of the thin film surrounding the elongated bubbles. A gradual decrease in h_{tp} is incurred with increasing x_e, with the portion of the channel incurring bubble nucleation gradually decreasing. An important heat transfer mechanism associated with the low quality regime is *intermittent dryout,* which is encountered by either formation of vapor blankets within the liquid slugs or partial dryout of the liquid film surrounding the elongated bubbles. Schematic (ii) depicts flow boiling in the mid quality region ($0.36 < x_e < 0.50$, $0.17 < X_{tt} < 0.31$, $9.4 < We^* < 12$). Here, annular flow prevails, with heat transfer dominated by convective boiling associated with heat transfer across the annular liquid film and interfacial evaporation. This is followed by the third, high quality region ($0.50 < x_e < 0.74$, $0.07 < X_{tt} < 0.17$, $12 < We^* < 15.7$) depicted in schematic (iii), which also consists of annular flow, but where h_{tp} begins to decrease sharply with increasing x_e. This decrease commences at the *dryout incipience* point, where the annular film begins to fully evaporate locally, exposing the wall directly to the vapor core. Mist flow is established for x_e > 0.74 corresponding to *dryout completion,*

downstream of which very mild cooling is possible from liquid droplets impacting the wall.

Following is a discussion of important transient characteristics of flow boiling in the crew and avionics HXs. It will be shown how the aforementioned mechanisms of intermittent dryout, dryout incipience and dryout completion influence these transients.

3.2. Transient heat transfer characteristics in crew HX (low x_e range)

3.2.1. Axial suppression of nucleate boiling and heat transfer degradation due to intermittent dryout

Fig. 4(a) shows the variation of h_{tp} with x_e along the crew HX for q''_{crew} = 32,291.7 W/m^2 and mass velocities in the range of G_{crew} = 264.63–529.25 kg/m^2 s. The heat transfer coefficient decreases monotonically with increasing x_e at a decreasing rate towards the downstream.

Figs. 4(b) show photo sequences of flow boiling along the crew HX for one of the cases shown in Fig. 4(a), q''_{crew} = 32,291.7 W/m^2 and G_{crew} = 378.04 kg/m^2 s, captured at three axial locations. For each axial location in Fig. 4(b), the last image on the left side is followed by the first image on the right. For z = 22.9 mm, corresponding to low x_e, Fig. 4(b) shows predominantly slug flow with heat transfer comprised of nucleate boiling inside liquid slugs and heat transfer across the liquid film surrounding the elongated bubble. The image sequence corresponding to z = 76.2 mm captures a marked decrease in liquid slug length and suppression of bubble nucleation within the liquid slug as the axial increase in x_e increases the length of the elongated bubble. The image sequence corresponding to z = 129.5 mm shows nucleation is virtually fully suppressed as transition to annular flow takes effect, but with remnants of the upstream slug flow regime acting as a *liquid wave* that propagates along the channel. Comparing these trends to the variation of h_{tp} with x_e in Fig. 4(a) for G_{crew} > 264.63 kg/m^2 s shows a direct correlation between the axial suppression of nucleation, coupled with transition to annular flow, and the axial decline in h_{tp}. Notice that intermittent dryout occurs at G_{crew} = 264.63 kg/m^2 s but not the three higher G_{crew} values. This shows that partial
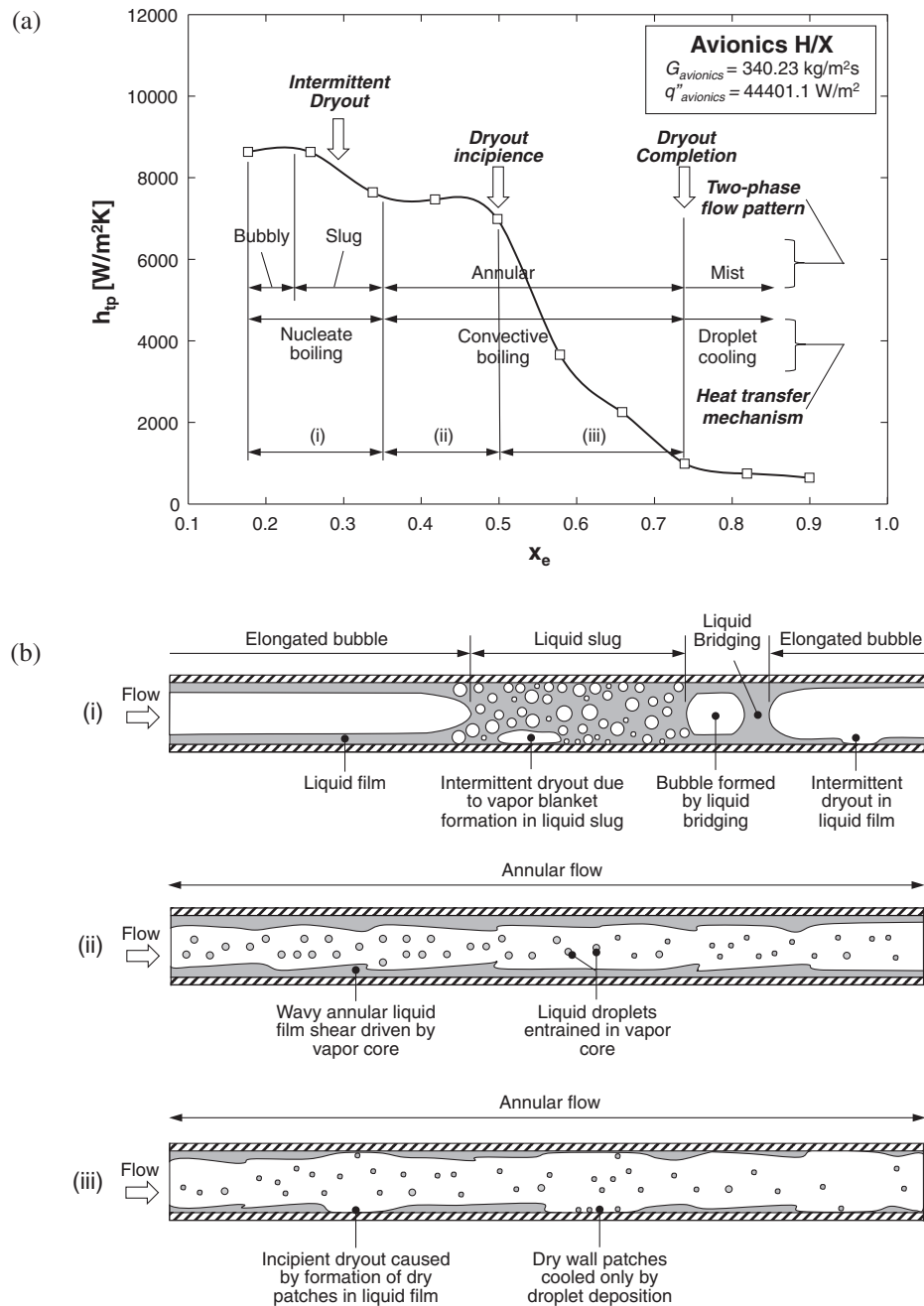
(a)

(b)

Fig. 3. (a) Variation of heat transfer coefficient with quality along avionics HX at $G_{avionics}$ = 340.23 kg/m² s and $q''_{avionics}$ = 44,401.1 W/m². (b) Schematics of flow boiling for the quality ranges in (a) illustrating dominant flow patterns and heat transfer mechanisms. Adapted from [25].

dryout inside the elongated liquid film, which occurs only for G_{crew} = 264.63 kg/m² s, is the primary cause for intermittent dryout.

Fig. 5(a) shows the variation of the heat transfer coefficient with x_e along the crew HX for a heat flux of q''_{crew} = 48,437.6 W/m² and mass velocities in the range of G_{crew} = 264.63–529.25 kg/m² s. Like the case for q''_{crew} = 32,291.7 W/m² in Fig. 4(a), the heat transfer coefficients in Fig. 5(a) are shown decreasing monotonically with increasing x_e. But because of the higher heat flux, intermittent dryout occurs at a relatively higher mass velocity of G_{crew} = 340.23 kg/m² s. Additionally, the quality corresponding to the onset of intermittent dryout is reduced from 0.2 to 0.15 as the heat flux is increased from 32,291.7 to 48,437.6 W/m². There is also a significant suppression of nucleation for x_e > 0.3 at

48,437.6 W/m². Intermittent dryout is not encountered for the higher mass velocities of G_{crew} = 378.04–529.25 kg/m² s.

Fig. 5(b) shows two image sequences corresponding to the same heat flux, q''_{crew} = 48,437.6 W/m², and two of the mass velocities in Fig. 5(a), G_{crew} = 264.63 and 378.04 kg/m² s. These two sequences are recorded in the upstream region of the channel at z = 22.9 mm, and individual images in each sequence are 3.125 ms apart. The sequence corresponding to G_{crew} = 264.63 kg/m² s, which is below the intermittent dryout value of 340.23 kg/m² s at z = 22.9 mm, shows the liquid film surrounding the elongated bubbles incurring partial dryout. On the other hand, the sequence corresponding to G_{crew} = 378.04 kg/m² s, which exceeds the intermittent dryout value at z = 22.9 mm, shows the liquid film is maintained until the arrival of the next liquid slug.
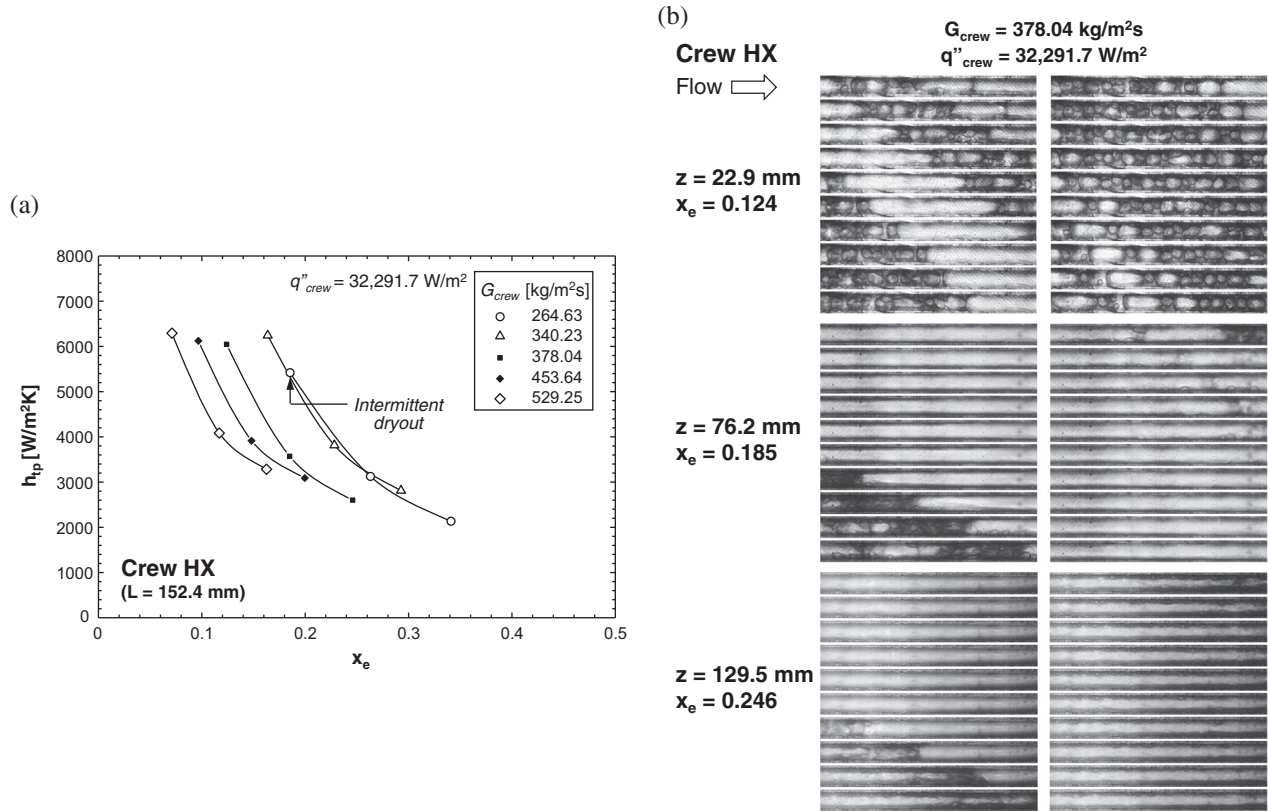
Fig. 4. (a) Variations of heat transfer coefficient with quality along crew HX for q''_{crew} = 32,291.7 W/m^2 and different mass velocities. (b) High speed image sequences of flow boiling in the crew HX for q''_{crew} = 32,291.7 W/m^2 and G_{crew} = 378.04 kg/m^2 s at z = 22.9, 76.2, and 129.5 mm. Time interval between individual images in each sequence is 2.5 ms.

It is important to note that, because of the relatively lower x_e values achieved in the crew HX, dryout incipience, which is associated with the high quality annular regime, is not encountered for the operating conditions of Figs. 4(a) and 5(a).

The intermittent dryout and dryout incipience mechanisms can be distinguished from one another by vapor quality, flow pattern, and the variation of h_{tp} with x_e. Intermittent dryout commences in a low quality region corresponding to transitions from slug to annular flow and nucleate to convective boiling, where liquid is abundant, so any dry patches inside the elongated bubble can be replenished in a short duration. On the other hand, dryout incipience commences in a high quality region corresponding to transition from annular to mist flow, where dry patches in the annular film continue to spread because of liquid deficiency. Differences between the intermittent dryout and dryout incipience mechanisms are also reflected in the variation of h_{tp} with x_e. Notice how the occurrence of intermittent dryout in the crew HX with decreasing G_{crew} in Figs. 4(a) and 5(a) does not alter the overall shape of the curve. However, Fig. 3(a) shows dryout incipience in the avionics HX precipitating a rapid and substantial decrease in h_{tp}.

3.3. Transient Heat transfer characteristics in avionics HX (low to high x_e range)

3.3.1. Heat flux trends for avionics HX

As indicated earlier, larger size and greater power input enables the avionics HX to span a much broader range of qualities compared to the crew HX. This also results in the avionics HX spanning drastically different heat transfer mechanisms, including nucleate boiling corresponding to mostly low quality slug flow, convective boiling associated by annular flow, and post dryout associated with downstream mist flow.

Fig. 6(a) shows variations of h_{tp} with x_e along the avionics HX for $G_{avionics}$ = 245.72 kg/m^2 s and heat fluxes of $q''_{avionics}$ = 12,109.4, 24,218.8 and 40,364.7 W/m^2. There is a stronger heat flux influence on h_{tp} in the low quality range, where the highest h_{tp} values are achieved due to dominance of nucleate boiling.

As in the crew HX, suppression of nucleate boiling in the avionics HX is associated with disappearance of liquid slugs and transition from nucleate boiling in the slug flow regime to convective boiling in the annular regime. This transition is clearly manifest in Fig. 6(a) for $q''_{avionics}$ = 24,218.8 W/m^2 at x_e = 0.375, where h_{tp} increases with increasing x_e due to convective boiling. In the annular regime associated with convective boiling, i.e., heat transfer across the liquid film, which is intensified with increased x_e as the liquid film grows thinner due to the combined effects of decreased liquid flow rate and increased vapor shear. Dryout incipience occurs when the liquid film dries out locally due to evaporation, causing h_{tp} to begin decreasing significantly with increasing x_e. Dryout incipience occurs at $q''_{avionics}$ = 12,109.4 and 24,218.8 W/m^2 but not 40,364.7 W/m^2. For $q''_{avionics}$ = 40,364.7 W/m^2, convective boiling enhancement that is triggered by liquid wave propagation moves upstream, so nucleate boiling and convective boiling occur simultaneously. This renders the two boiling mechanisms difficult to distinguish from one another, and helps explain why the h_{tp} versus x_e data corresponding to $q''_{avionics}$ = 40,364.7 W/m^2 feature a smooth monotonic decrease with no clear sign of dryout incipience.

Fig. 6(b) shows flow boiling images of three adjacent microchannels at three axial locations of z = 44.2, 275.8 and 565.4 mm along the avionics HX corresponding to the same mass velocity and heat fluxes as Fig. 6(a). For all three heat fluxes, there is a
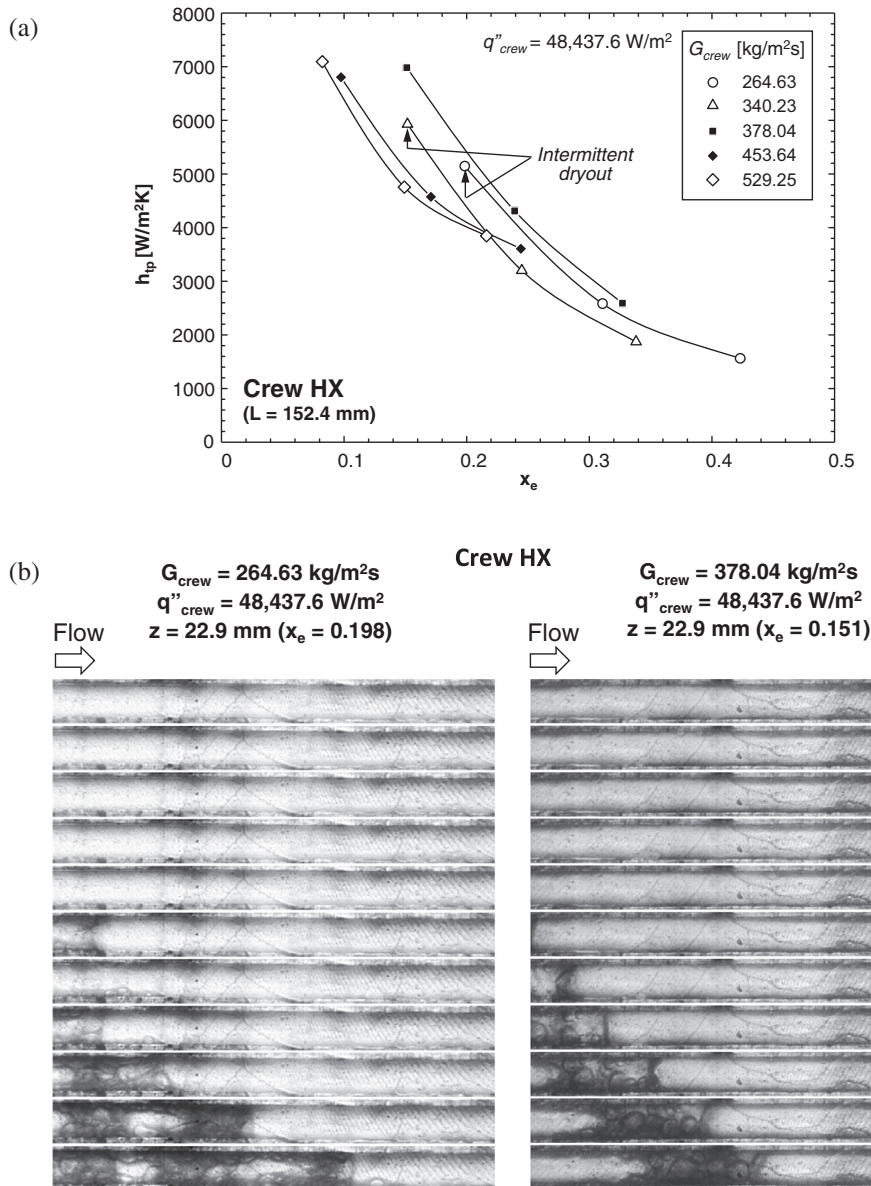
Fig. 5. (a) Variations of heat transfer coefficient with quality along crew HX for q''_{crew} = 48,437.6 W/m² and different mass velocities. (b) High speed image sequences at z = 22.9 mm for q''_{crew} = 48,437.6 W/m² and two mass velocities. Time interval between images in each sequence is 3.125 ms.

gradual transition from slug flow upstream to annular flow, followed by annular flow with partial dryout. However, the highest heat flux case of $q''_{avionics}$ = 40,364.7 W/m² is shown culminating in complete dryout downstream.

3.3.2. Liquid wave propagation along avionics HX

Fig. 7(a) captures details of the transition from slug to annular flow. Shown are image sequences corresponding to $G_{avionics}$ = 245.72 kg/m² s and $q''_{avionics}$ = 24,218.8 W/m² captured at four axial locations along the avionics HX of z = 44.2, 102.1, 160.0, and 275.8 mm. Thirteen sequential images capture the two-phase flow in one micro-channel, and individual images are 0.625 ms apart. A flow regime consisting of liquid slugs and elongated bubbles at z = 44.2 mm is converted into predominantly annular flow at z = 102.1 mm, but with remnants of the liquid slugs mimicking a *liquid wave*. The liquid wave propagates at a speed slightly slower than that of the vapor core but much faster than the annular film, and the intensity of the liquid wave is mitigated by evaporation and momentum loss due to friction as it flows downstream to

z = 160.0 mm. Notice how the liquid wave serves to partially preserve nucleate boiling at z = 102.1 and 160.0 mm, but virtually disappears around the middle of the avionics HX, z = 275.8 mm; this is where h_{tp} begins to drop sharply until the liquid film eventually dries out completely. It should be noted that temporal differences in flow behavior are observed among the parallel channels in the heat sink because of the combined effects of flow instabilities and slight differences in flow distribution at the inlet.

Notice in Fig. 6(a) the monotonic decrease in h_{tp} with increasing x_e for $G_{avionics}$ = 245.72 kg/m² s and highest heat flux of $q''_{avionics}$ = 40,364.7 W/m². Absent for this set of conditions is (i) the nucleate boiling enhancement in the lower quality range, x_e < 0.4, (which is clearly captured for $q''_{avionics}$ = 24,218.8 W/m²), (ii) the decrease in h_{tp} due to intermittent dryout, and (iii) the ensuing increase in h_{tp} due to transition to annular flow and convective boiling.

Overall, the liquid waves are intensified at z = 44.2 and 102.1 mm for $q''_{avionics}$ = 40,364.7 W/m², Fig. 7(b), compared to the liquid wave at $q''_{avionics}$ = 24,218.8 W/m², Fig. 7(a). Fig. 7(b) shows
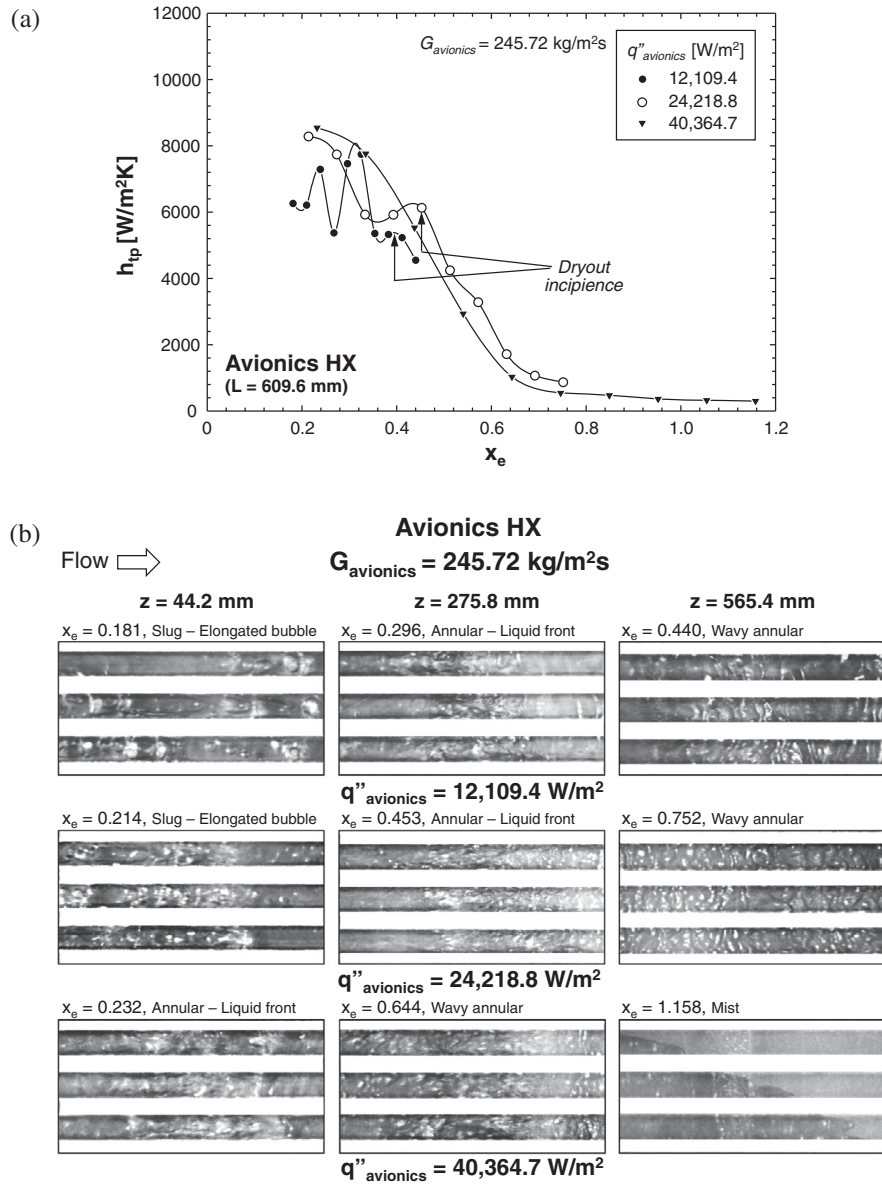
(a)

(b)

Fig. 6. (a) Variations of heat transfer coefficient with quality along avionics HX for $G_{avionics}$ = 245.72 kg/m² s and three heat fluxes. (b) Flow boiling images of three adjacent micro-channels at three axial locations along avionics HX corresponding to same mass velocity and heat fluxes as (a).

the liquid wave at the higher flux is rapidly consumed by evaporation as it passes over the dry wall patches after dryout incipience.

Fig. 8 shows a schematic representation of the wetting and dryout periods after dryout incipience. Nucleate boiling can occur within the short liquid waves, providing partial cooling, especially within dry portions of the wall in the predominantly annular flow regime associated with convective boiling. The mass of liquid wave is gradually reduced until it is fully consumed. This is where the dry wall patches associated with incipient dryout increase sharply in both axial length and frequency, resulting in the observed sharp downstream decrease in h_{tp}. The liquid droplets entrained in the vapor core delay complete dryout of the liquid film during transition to mist flow.

3.3.3. Mass velocity trends for avionics HX

Fig. 9(a) shows the variations of h_{tp} with x_e along the avionics HX for $q''_{avionics}$ = 24,218.8 W/m² and three mass velocities. The dryout incipience point is shown shifted to higher qualities and

farther downstream locations with increasing $G_{avionics}$, which suggests that dryout incipience is influenced by liquid momentum.

Fig. 9(b) shows images of flow boiling in three adjacent micro-channels for the same heat flux and mass velocities as Fig. 9(a) and three axial locations. For $G_{avionics}$ = 170.11 kg/m² s, flow regime is shown changing from slug at z = 44.2 mm, to wavy annular at z = 275.8 mm, and complete dryout (mist flow) at z = 565.4 mm. Increasing $G_{avionics}$ to 245.72 kg/m² s results in slug flow at z = 44.2 mm, followed by annular flow with liquid wave for z = 275.8, and wavy annular flow at z = 565.4 mm; where the wavy annular regime is free from propagating liquid waves. Notice how increasing mass velocity serves to sustain annular flow at the downstream location, where $G_{avionics}$ = 170.11 kg/m² s results in complete dryout. Increasing $G_{avionics}$ to 321.33 kg/m² s, wavy annular flow is maintained to the end of the channel, preventing complete dryout.

The role of the liquid wave can be assessed by examining h_{tp} curves in Fig. 9(a) and the three images for z = 275.8 mm in Fig. 9 (b). The convective boiling enhancement effect is observed for
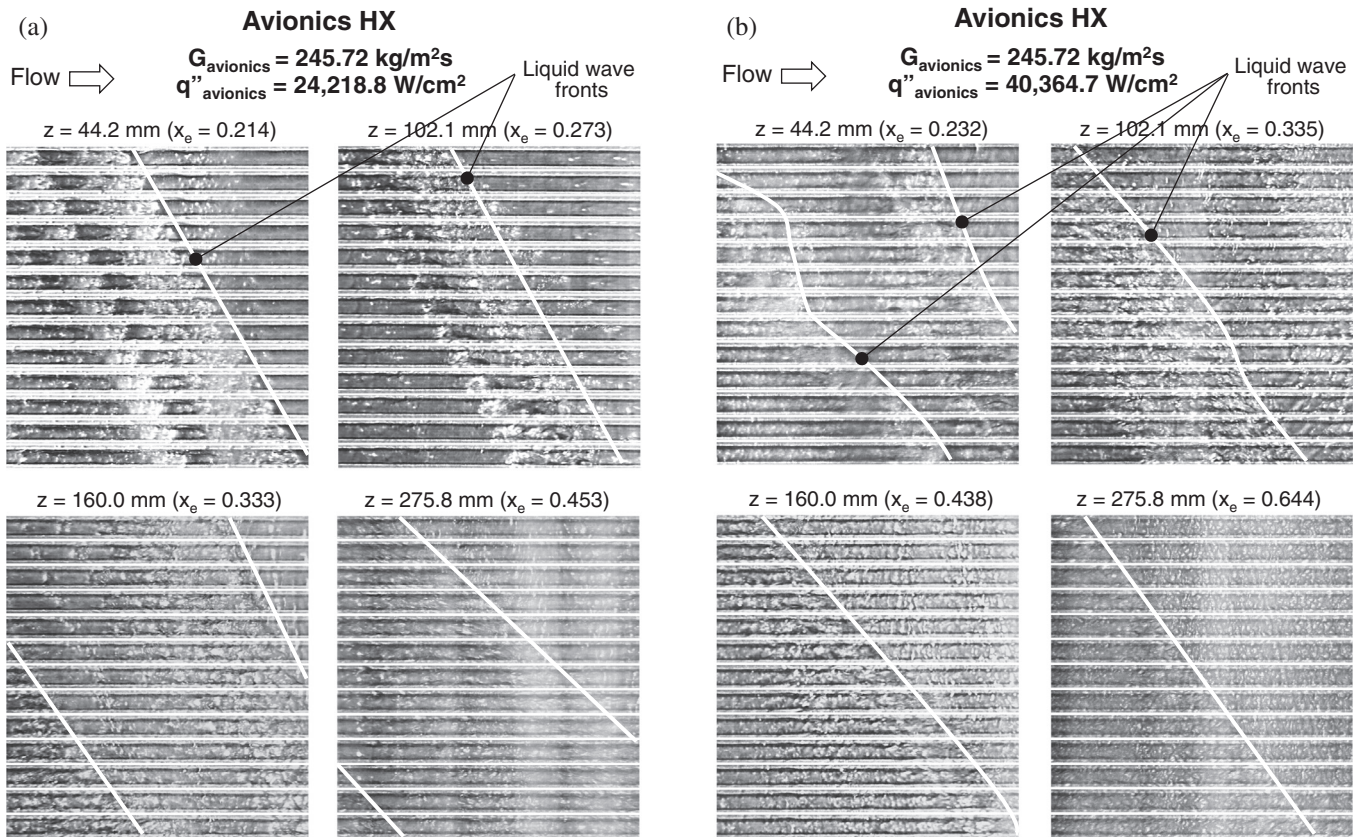
Fig. 7. Image sequences capturing liquid wave propagation during transition from slug to annular flow at four axial locations along avionics HX for $G_{avionics}$ = 245.72 kg/m^2 s and (a) $q''_{avionics}$ W/m^2, and (b) $q''_{avionics}$ = 40,364.7 W/m^2. Individual images in each sequence are 0.625 ms apart.
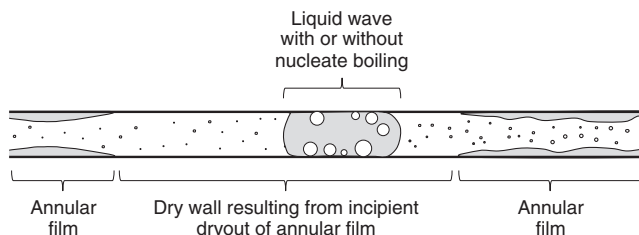

Fig. 8. Schematic illustration of liquid wave propagation within dry wall portion of annular flow region following incipient dryout.

the two highest mass velocities, presumably because of the influence of the liquid wave in annular flow, while the convective boiling enhancement is nonexistent for the lowest mass velocity of $G_{avionics}$ = 170.11 kg/m^2 s without the liquid wave.

Fig. 9(a) and (b) also show the influence of mass velocity on liquid wave propagation. Increasing $G_{avionics}$ increases travel distance of the liquid wave, so the dryout incipience point is also shifted downstream as shown in Fig. 9(a). Additionally, a minimum mass velocity is required to initiate the liquid wave in annular flow, with no signs of the liquid wave observed anywhere for the lowest mass velocity of $G_{avionics}$ = 170.11 kg/m^2 s.

4. Parallel-channel instability and pressure drop fluctuations

4.1. Pressure drop fluctuations in time domain

As indicated earlier, Qu and Mudawar [19] captured two types of instability associated with flow boiling in heat sinks containing

parallel micro-channels: large amplitude pressure-drop oscillation, and mild parallel-channel instability. By throttling the flow upstream of the heat sink with the aid of a control valve, they were able to eliminate the pressure-drop oscillation but not the parallel-channel instability.

The two control valves mounted upstream of the crew HX in the present study served a similar throttling purpose, eliminating the pressure-drop oscillation but not the parallel-channel instability. To capture the latter instability, pressure drop is recorded in the present study over a sampling duration of 367.658 s. Fig. 10(a) shows pressure measurements at the inlet and outlet of the crew HX for G_{crew} = 264.63 kg/m^2 s and q''_{crew} = 16,146.9 W/m^2 over 100 s of the 367.658-s duration. Because of the high stiffness provided by the throttling valves, the inlet pressure undergoes less fluctuation than the downstream pressure, while the latter shows more significant fluctuation resulting from passage of the density wave associated with the parallel-channel instability. Fig. 10(b) shows the corresponding pressure drop fluctuations across the crew HX. This pressure drop sample has a maximum amplitude of about 12,000 Pa and resembles the parallel-channel instability records of Qu and Mudawar in both small amplitude and short fluctuation period; with periods ranging from 1.32 to 1.41 s and averaging 1.3569 s.

To better understand the relationship between these pressure fluctuations and flow patterns, high speed video is used to capture the interfacial behavior in the middle of the micro-channel, z = 76.2 mm. Video analysis shows two distinct periods characterized by drastically different flow behavior. The total period of events captured on video is 1358.250 ms while pressure drop fluctuation period ranges from 1320.0 to 1410.0 ms. Repeated in succession are a *liquid-deficient period* and a *liquid-abundant period*.
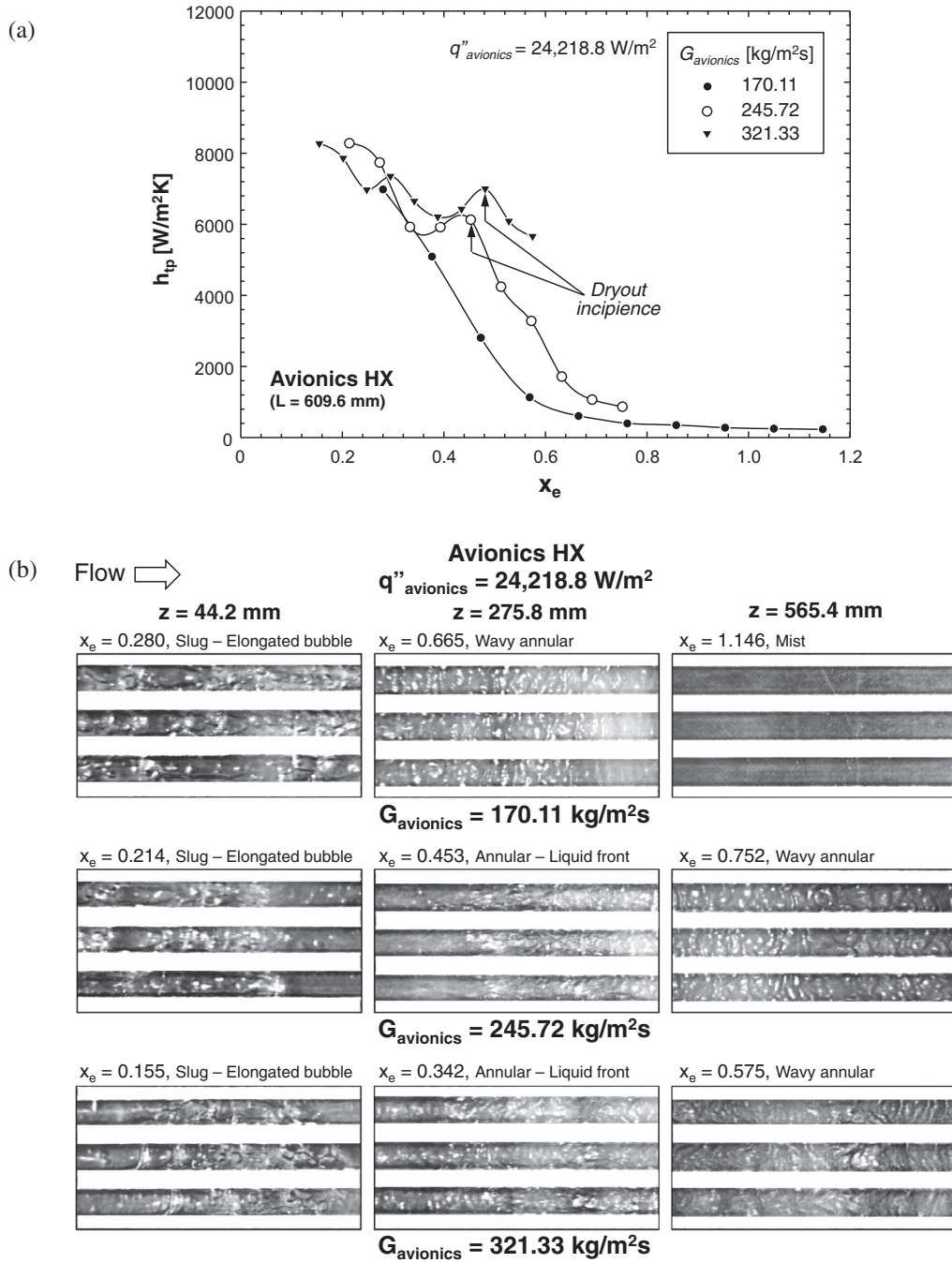
Fig. 9. (a) Variations of heat transfer coefficient with quality along avionics HX for $q''_{avionics}$ = 24,218.8 W/m² and three mass velocities. (b) Flow boiling images of three adjacent micro-channels at three axial locations along avionics HX corresponding to same heat flux and mass velocities as (a).

Fig. 10(c) shows, for the same mass velocity and heat flux as Fig. 10(b), representative images for each period captured at 0 and 679.125 ms of the 1358.250-ms period. The top image, which is representative of the liquid-deficient period, depicts an elongated slug flow bubble with surrounding liquid film undergoing evaporation; the front and tail of the elongated bubble are located outside of the frame. The lower image, representative of the liquid-abundant period, depicts a liquid slug in the same slug flow regime undergoing nucleate boiling; consecutive liquid slugs appear at the same location within the liquid-abundant period every 50–100 ms. It is important to note that the top image, which is representative of the liquid-deficient period, is associated with a low pressure

drop period compared to high pressure drop period for the bottom liquid-abundant image.

4.2. Pressure drop fluctuations in frequency domain

To analyze the pressure drop response in frequency domain, a discrete Fourier transform is applied to the data in Fig. 10(b). The pressure drop time record is expressed in complex form of Fourier series as [27]

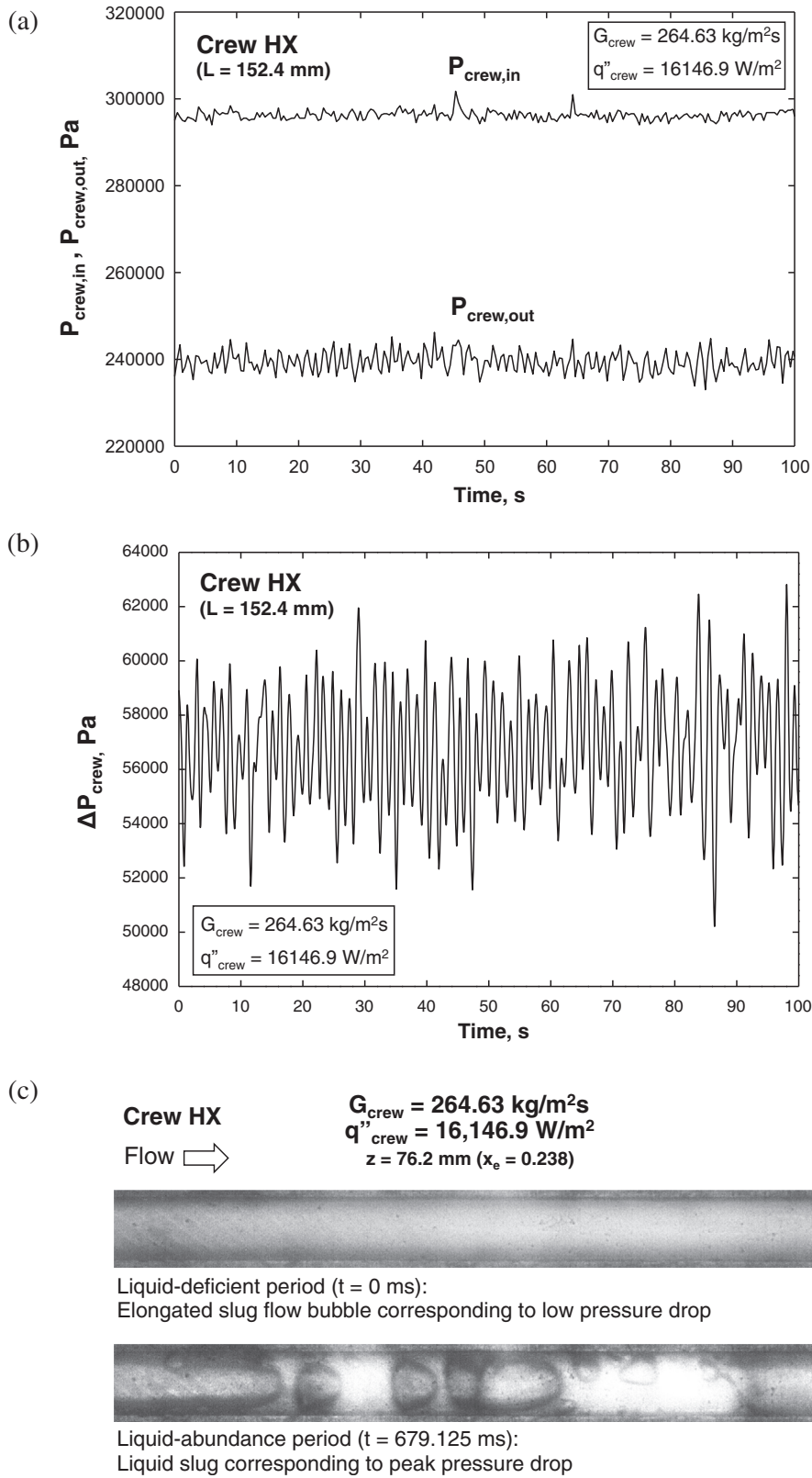$$f_k = f(x_k) = \sum_{n=0}^{N-1} C_n e^{-inx_k}, \qquad (4)$$

(a)

(b)

(c)

Crew HX

Flow ⟹

G_{crew} = 264.63 kg/m²s
q''_{crew} = 16,146.9 W/m²
z = 76.2 mm (x_e = 0.238)

Liquid-deficient period (t = 0 ms):
Elongated slug flow bubble corresponding to low pressure drop

Liquid-abundance period (t = 679.125 ms):
Liquid slug corresponding to peak pressure drop

Fig. 10. Temporal records of crew HX's (a) inlet and outlet pressure signals and (b) pressure drop for G_{crew} = 264.63 kg/m² s and q''_{crew} = 16,146.9 W/m², and (c) flow images corresponding to low and peak pressure drop captured at z = 76.2 mm.

where x_k represents the sampling points in time, expressed as

$$x_k = \frac{2\pi k}{N}, \quad k = 0, 1, \ldots, N-1 \qquad (5)$$

N the total number of measurement points, and C_n the complex Fourier coefficient of f_k at a sampling frequency of $2\pi kn/N$. C_n is expressed as

$$C_n = \frac{1}{N}\sum_{k=0}^{N-1} f_k e^{-inx_k}, \quad n = 0, 1, \ldots, N-1 \tag{6}$$

The discrete Fourier transform is expressed as

$$\hat{f}_n = NC_n = \sum_{k=0}^{N-1} f_k e^{-inx_k}, \quad n = 0, 1, \ldots, N-1 \tag{7}$$

With the sampling rate is 0.4280 s (corresponding to a sampling frequency of $F_s = 1/0.4280 = 2.3364$ Hz) the Nyquist frequency is $F_{Nyq} = F_s/2 = 1.1682$ Hz.

The average power spectrum is calculated according to

$$\overline{P} = \frac{1}{N}\sum_{n=0}^{N-1} \hat{f}_n \hat{f}_n^*, \quad n = 0, 1, \ldots, N-1 \tag{8}$$

where f_n^* is the complex conjugate of Fourier transform, and the total number of sampling points is $N = 860$ for 367.658 s. The averaged power spectrum of the crew HX's pressure drop fluctuations from Fig. 10(b) is shown in Fig. 11. The highest pressure spectrum is achieved at 0.737 Hz, so the pressure drop fluctuation frequency is lower than the Nyquist frequency of $F_{Nyq} = 1.168$ Hz. This implies the sampling rate is fast enough to capture the pressure drop fluctuation and avoid the lower frequency alias. The fluctuation period measured by the average power spectrum is $1/(0.737$ Hz$) = 1.3569$ s, which is almost equal to the average period in time domain of video capture of 1.358.25 s.

It can therefore be concluded that mass flow rate and pressure drop are closely correlated and possess a frequency that changes for different operating conditions such as heat flux, mass flow rate, inlet quality, and channel dimensions [21]. More research is required to investigate variations of the fluctuation frequency for micro-channel flow boiling under different operating conditions.

5. Assessment of flow regime maps

Five different flow regime maps are examined for effectiveness in predicting the flow regimes captured in the present study. The five maps include those intended for adiabatic, boiling, and condensing flows. Table 3 provides details of the individual maps, including working fluids and the map's coordinate parameters.

Mandhane's [28] adiabatic flow regime map has been widely used for air/water flow in macro-channels with $D_h = 12.7$–165.1 mm. These maps employ superficial liquid velocity, j_f, and superficial vapor velocity, j_g, as coordinate parameters. To extend the applicability of the map to other fluids, it is imperative to account for the huge density differences between those of the
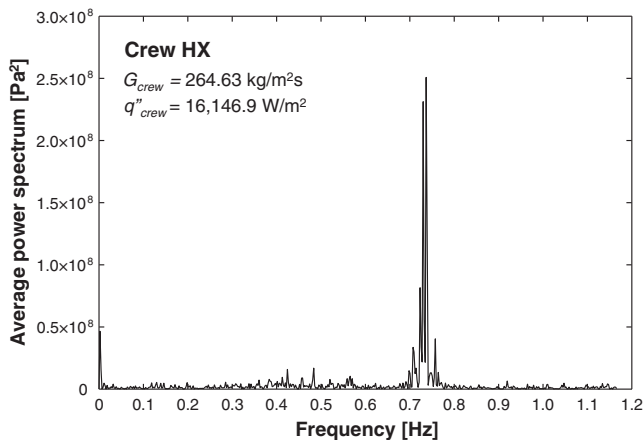

Fig. 11. Average power spectrum of pressure drop fluctuations in crew HX in frequency domain for $G_{crew} = 264.63$ kg/m² s and $q''_{crew} = 16,146.9$ W/m².

working fluid and air/water. Several parameters have been proposed to correct superficial velocity for these density differences, including replacing j_g by

$$j_{g,cor} = \sqrt{\rho_g/\rho_{air}}j_g, \tag{9}$$

[33,34], which is proportional to the square root of superficial vapor momentum. Fig. 12(a) shows the flow regimes captured in the present study superimposed on the Mandhane map modified by replacing j_g by $j_{b,cor}$. Overall, the map does capture the general flow regime trends of the present study, but with significant departure along the boundary between slug and annular flow. A key weakness of the Mandhane map is the use of dimensional parameters that fail to account for such important parameters as surface tension and channel diameter [35].

Flow regime maps utilizing dimensionless parameters are better able to account for thermophysical properties of different working fluids as well as different hydraulic diameters. Popular dimensionless groups in these maps include turbulent–turbulent Lockhart–Martinelli parameters, X_{tt}, and modified Weber number, We^*, which have been recommended for horizontal flow condensation to account for effects of surface tension, viscosity, and vapor momentum [29,30]. The Lockhart–Martinelli parameter is defined as

$$X_{tt} = \left(\frac{\mu_f}{\mu_g}\right)^{0.1} \left(\frac{1-x}{x}\right)^{0.9} \left(\frac{v_f}{v_g}\right)^{0.5} \tag{10}$$

A modified Weber number was proposed by Soliman [36] to account for the ratio of the destructive vapor inertia to the stabilizing effects of surface tension and liquid viscosity. The modified Weber number is expressed in terms of the Suratman number, Su_g, as

$$We^* = 2.45\frac{Re_g^{0.64}}{Su_g^{0.3}\left(1 + 1.09X_{tt}^{0.039}\right)^{0.4}} \quad \text{for } Re_f \leqslant 1250, \tag{11a}$$

and

$$We^* = 0.85\frac{Re_g^{0.79}X_{tt}^{0.157}}{Su_g^{0.3}\left(1 + 1.09X_{tt}^{0.039}\right)^{0.4}} \left[\left(\frac{\mu_g}{\mu_f}\right)^2 \left(\frac{v_g}{v_f}\right)\right]^{0.084}$$
$$\text{for } Re_f > 1250, \tag{11b}$$

where

$$Re_g = \frac{xGD}{\mu_g}, \tag{12a}$$

$$Re_f = \frac{(1-x)GD}{\mu_f}, \tag{12b}$$

and

$$Su_g = \frac{\rho_g \sigma D}{\mu_g^2} \tag{13}$$

Both Soliman [29] and Chen et al. [30] showed that flow regime transitions depend on We^* alone. However, Fig. 12(b) shows the transitions between the flow regimes of the present study vary with both We^* and X_{tt}. The transition from slug to annular flow is shown increasing with increasing X_{tt}. Small channel size in the present study may explain the departure of present flow regime transitions from those of Soliman and Chen et al.

Fig. 12(c) superimposes the present flow regime data on a flow regime map recommended recently by Revellin et al. [31] for micro-channel flows, which uses mass velocity, G, and vapor quality, x, as coordinate parameters. In this map, slug flow is considered

Table 3
Details of prior flow regime maps.

Author(s)	Coordinate parameters	Channel size	Flow type	Fluid(s)	Remarks
Mandhane et al. [28]	j_f versus j_g	Macro-channel	Adiabatic	Air/water	Circular: D_h = 12.7–165.1 mm
Soliman [29]	We^* versus X_{tt}	Macro-channel	Condensing	Steam, R113, R12	Circular: D_h = 7.4–12.7 mm
Chen et al. [30]	We^* versus X_{tt}	Macro-channel	Condensing	R134a	Circular: D_h = 12, 14 mm
Revellin and Thome [31]	G versus x	Micro-channel	Boiling	R134a, R245fa	Circular: D_h = 0.509, 0.790 mm
Kim and Mudawar [32]	We^* versus X_{tt}	Micro-channel	Condensing	FC-72	Rectangular: D_h = 1 mm
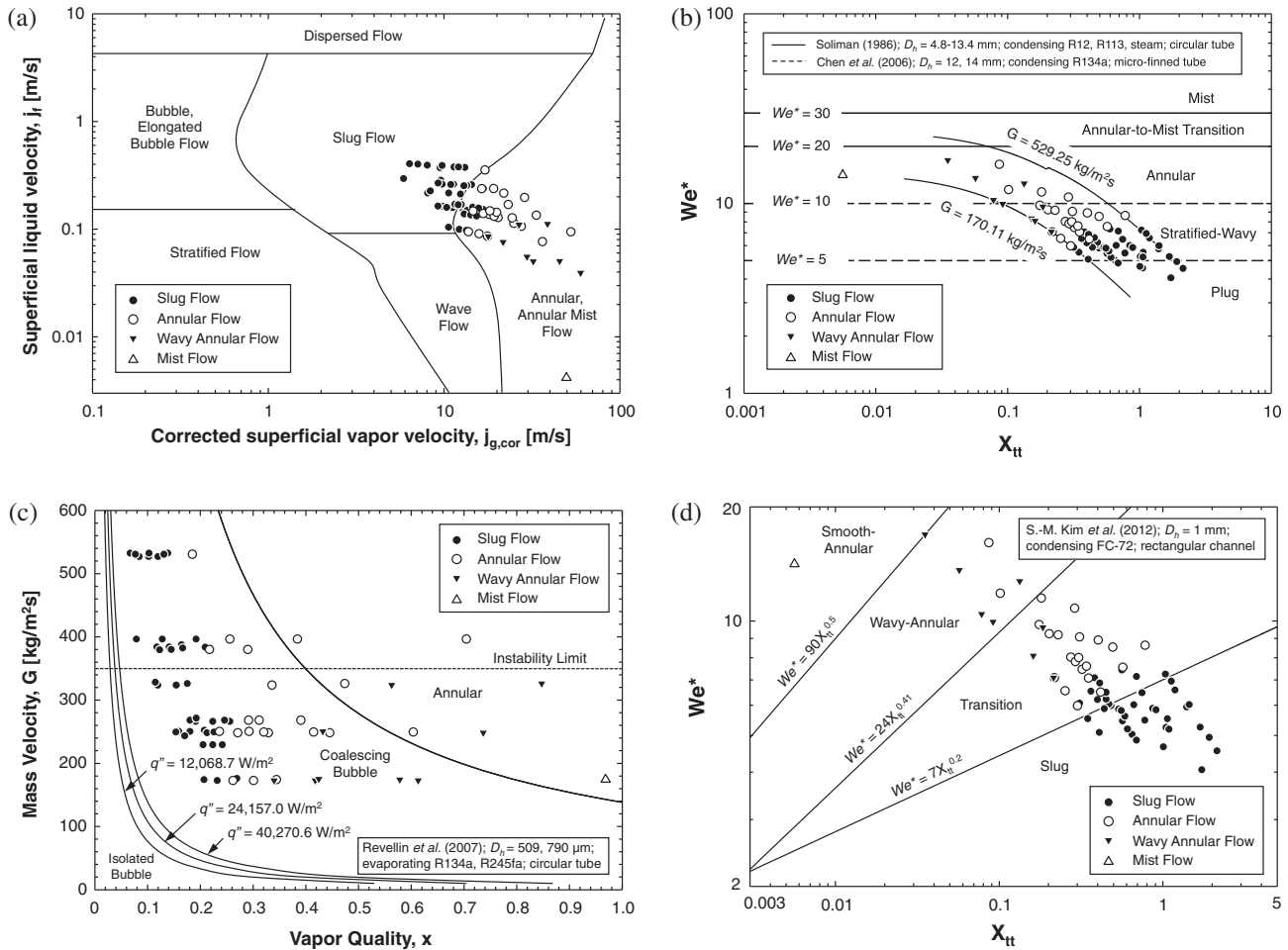
Fig. 12. Present flow regime data superimposed on flow regime maps of (a) Mandhane et al., (b) Soliman and Chen et al., (c) Revellin and Thorme, and (d) Kim and Mudawar.

part of coalescing bubble flow. Both slug flow and most annular flow data are shown falling into the map's coalescing bubble flow region. Deviations between the present flow regimes and the Revellin et al. map are attributed to the map's reliance on dimensional parameters, which limits its applicability to different working fluids and other channel shapes and sizes.

Fig. 12(d) superimposes the present flow regime data on a flow regime map recommended by Kim and Mudawar [32] for FC-72 condensation in micro-channels. This map is an attempt to correct the dependence of flow regime transitions on We^* and X_{tt} missed with the transition lines of Soliman and Chen et al. as shown in Fig. 12(b). The map in Fig. 12(d) uses the following flow regime boundaries:

$$\text{Smooth-annular to wavy-annular}: \quad We^* = 90 X_{tt}^{0.5} \quad (14a)$$

$$\text{Wavy-annular to transition}: \quad We^* = 24 X_{tt}^{0.41} \quad (14b)$$

$$\text{Transition to slug}: \quad We^* = 7 X_{tt}^{0.2} \quad (14c)$$

This map shows general agreement with the present data especially in the transition region. However, deviations are expected given that the map was intended for condensing flows and cannot capture the complexities of flow boiling discussed earlier in this study.

Overall, future efforts concerning flow regime determination must relay on better mechanistic descriptions of flow boiling behavior. This endeavor will require the use of more sophisticated diagnostic tools to better understand the important role of interfacial waves [37,38] and measure such illusive parameters as instantaneous thickness and velocity profile of the liquid film in the slug and annular flow regimes. Details of these important diagnostic methods are available in [39–43].

6. Conclusions

This study investigated both time-averaged and transient characteristics of large area micro-channel evaporators incorporated in an R-134a vapor compression loop. Two separate micro-channel evaporators were used, a crew HX and an avionics HX. The shorter

and lower power crew HX produced relatively low exit qualities of 0.1191–0.5298, while the avionics HX yielded both low and high exit qualities of 0.4071–1.5677. Local heat transfer coefficient trends for both evaporators were investigated for different mass velocities and heat fluxes, and flow regime trends for representative operating conditions were examined with high-speed video. The video records provided crucial information concerning dominant flow regimes and heat transfer mechanisms at different axial locations along each evaporator. In addition, temporal records of pressure drop across the crew HX were examined in both time and frequency domains to better understand flow related instabilities. The combination of heat transfer data, video records and pressure drop response provided valuable insight into important transient fluid flow and heat transfer characteristics of the two evaporators. Finally, previous flow regime maps were assessed for accuracy in predicting the observed flow patterns. Key conclusions from the study can be summarized as follows.

(1) Relatively low qualities result in two-phase flow along the crew HX dominated by slug flow and nucleate boiling. Here, heat is transferred by both nucleate boiling within the liquid slugs and evaporation of the film surrounding the elongated bubbles. Increasing quality precipitates a monotonic decrease in the heat transfer coefficient, which results mostly from decreasing length of the liquid slugs. With further increase in heat flux, heat transfer is eventually compromised by intermittent dryout resulting from localized vapor blanket formation in the liquid slugs and/or local dryout of the film surrounding the elongated bubbles.

(2) Given its broad range of qualities, the avionics HX is associated with different flow regimes and heat transfer mechanisms depending on quality range. Low qualities are associated with slug flow and dominated by nucleate boiling, while high qualities feature mostly annular flow, which is dominated by convective boiling. Further increases in quality trigger incipient dryout of the annular film, causing a sharp decrease in the heat transfer coefficient and a transition to mist flow downstream. An important transient phenomenon that influences both fluid flow and heat transfer along the avionics HX is a liquid wave composed of remnants of liquid slugs from the slug flow regime. In the slug flow regime, the liquid waves consist of longer liquid slugs that tend to overcome any localized wall exposure to the vapor resulting from intermittent dryout, which reduces the detrimental influence of this form of dryout. On the other hand, the liquid wave suffers significant loss of liquid as it enters the annular flow region, which greatly compromises its ability to replenish dry wall regions resulting from incipient dryout, rendering this form of dryout far more detrimental.

(3) Two-phase flow in the two evaporators shows clear signs of parallel-channel instability along the flow channels. Representative records for pressure drop across the crew HX reveal this instability is associated with fluctuations ranging from 1.32 to 1.41 s. A discrete Fourier transform of the pressure drop time record shows mass flow rate and pressure drop are closely correlated and possess a frequency that changes for different operating conditions such as heat flux, mass flow rate, inlet quality, and channel dimensions.

(4) Five different flow regime maps are assessed for accuracy in predicting flow regime transitions in the crew and avionics HXs. They include maps intended for both macro- and micro-channels and relying on both dimensional and non-dimensional parameters. Relatively good agreement is realized with a recent map by Kim and Mudawar [32] utilizing a modified Weber number along with the Lockhart–Martinelli parameter.

References

[1] F.P. Chiaramonte, J.A. Joshi, Workshop on critical issues in microgravity fluids, transport, and reaction processes in advanced human support technology – final report, NASA Report TM-2004-212940, 2004.

[2] S.H. Lee, I. Mudawar, M.M. Hasan, Thermal analysis of hybrid single-phase, two-phase and heat pump thermal control system (TCS) for future spacecraft, Appl. Therm. Eng. 100 (2016) 190–214.

[3] B.S. Singh, M.H. Hasan, Innovative multi-environment, multimode thermal control system, SAE Paper 2007-01-3202, 2007.

[4] I. Mudawar, Two-phase micro-channel heat sinks: theory, applications and limitations, J. Electron. Packag. – Trans. ASME 133 (2011) 041002-2.

[5] S.M. Kim, I. Mudawar, Universal approach to predicting saturated flow boiling heat transfer in mini/micro-channels part I. Dryout incipience quality, Int. J. Heat Mass Transfer 64 (2013) 1226–1238.

[6] S.M. Kim, I. Mudawar, Universal approach to predicting saturated flow boiling heat transfer in mini/micro-channels part II. Two-phase heat transfer coefficient, Int. J. Heat Mass Transfer 64 (2013) 1239–1256.

[7] Y.Y. Hsu, On the size range of active nucleation cavities on a heating surface, J. Heat Transfer – Trans. ASME 84 (1962) 207–213.

[8] P.A. Kew, K. Cornwell, Correlations for the prediction of boiling heat transfer in small-diameter channels, Appl. Therm. Eng. 17 (1997) 705–715.

[9] S. Lin, P.A. Kew, K. Cornwell, Two-phase heat transfer to a refrigerant in a 1 mm diameter tube, Int. J. Refrig. 24 (2001) 51–56.

[10] S. In, S. Jeong, Flow boiling heat transfer characteristics of R123 and R134a in a micro-channel, Int. J. Multiphase Flow 35 (2009) 987–1000.

[11] W. Qu, I. Mudawar, Flow boiling heat transfer in two-phase micro-channel heat sinks––I. Experimental investigation and assessment of correlation methods, Int. J. Heat Mass Transfer 46 (2003) 2755–2771.

[12] J. Lee, I. Mudawar, Two-phase flow in high-heat-flux micro-channel heat sink for refrigeration cooling applications: Part II—heat transfer characteristics, Int. J. Heat Mass Transfer 48 (2005) 941–955.

[13] H.J. Lee, S.Y. Lee, Heat transfer correlation for boiling flows in small rectangular horizontal channels with low aspect ratios, Int. J. Multiphase Flow 27 (2001) 2043–2062.

[14] S. Saitoh, H. Daiguji, E. Hihara, Effect of tube diameter on boiling heat transfer of R-134a in horizontal small-diameter tubes, Int. J. Heat Mass Transfer 48 (2005) 4973–4984.

[15] C.B. Tibiriçá, G. Ribatski, Flow boiling heat transfer of R134a and R245fa in a 2.3 mm tube, Int. J. Heat Mass Transfer 53 (2010) 2459–2468.

[16] M. Ducoulombier, S. Colasson, J. Bonjour, P. Haberschill, Carbon dioxide flow boiling in a single microchannel – Part II: heat transfer, Exp. Therm. Fluid Sci. 35 (2011) 597–611.

[17] H.Y. Wu, P. Cheng, Visualization and measurements of periodic boiling in silicon microchannels, Int. J. Heat Mass Transfer 46 (2003) 2603–2614.

[18] C. Huh, J. Kim, M.H. Kim, Flow pattern transition instability during flow boiling in a single microchannel, Int. J. Heat Mass Transfer 50 (2007) 1049–1060.

[19] W. Qu, I. Mudawar, Transport phenomena in two-phase micro-channel heat sinks, J. Electron. Packag. – Trans. ASME 126 (2004) 213–224.

[20] G. Yadigaroglu, A.E. Bergles, Fundamental and higher-mode density-wave oscillations in two-phase flow, J. Heat Transfer – Trans. ASME 94 (1972) 189–195.

[21] Y. Ding, S. Kakaç, X.J. Chen, Dynamic instabilities of boiling two-phase flow in a single horizontal channel, Exp. Therm. Fluid Sci. 11 (1995) 327–342.

[22] P. Saha, M. Ishii, N. Zuber, An experimental investigation of the thermally induced flow oscillations in two-phase systems, J. Heat Transfer – Trans. ASME 98 (1976) 616–622.

[23] H.C. Ünal, The period of density-wave oscillations in forced convection steam generator tubes, Int. J. Heat Mass Transfer 25 (1982) 419–421.

[24] K.H. Chang, C. Pan, Two-phase flow instability for boiling in a microchannel heat sink, Int. J. Heat Mass Transfer 50 (2007) 2078–2088.

[25] S. Lee, I. Mudawar, Investigation of flow boiling in large micro-channel heat exchanger in a refrigeration loop for space applications, Int. J. Heat Mass Transfer 97 (2016) 110–129.

[26] T.L. Bergman, F.P. Incropera, A.S. Lavine, D.P. DeWitt, Fundamentals of Heat and Mass Transfer, 7th ed., Wiley and Sons, New York, 2011.

[27] E. Kreyszig, Advanced Engineering Mathematics, 9th ed., John Wiley & Sons, New York, 2006.

[28] J.M. Mandhane, G.A. Gregory, K. Aziz, A flow pattern map for gas—liquid flow in horizontal pipes, Int. J. Multiphase Flow 1 (1974) 537–553.

[29] H.M. Soliman, The mist-annular transition during condensation and its influence on the heat transfer mechanism, Int. J. Multiphase Flow 12 (1986) 277–288.

[30] Q. Chen, R.S. Amano, M. Xin, Experimental study of flow patterns and regimes of condensation in horizontal three-dimensional micro-fin tubes, Heat Mass Transfer 43 (2006) 201–206.

[31] R. Revellin, J.R. Thome, A new type of diabatic flow pattern map for boiling heat transfer in microchannels, J. Micromech. Microeng. 17 (2007) 788–796.

[32] S.-M. Kim, I. Mudawar, Flow condensation in parallel micro-channels – Part 2: heat transfer results and correlation technique, Int. J. Heat Mass Transfer 55 (2012) 984–994.

[33] M.K. Dobson, J.C. Chato, Condensation in smooth horizontal tubes, J. Heat Transfer – Trans. ASME 120 (1998) 193–213.

[34] A. Cavallini, G. Censi, D.D. Col, L. Doretti, G.A. Longo, L. Rossetto, Condensation of halogenated refrigerants inside smooth tubes, HVAC&R Res. 8 (2002) 429–451.

[35] Y. Taitel, A.E. Dukler, A model for predicting flow regime transitions in horizontal and near horizontal gas–liquid flow, AIChE J. 22 (1976) 47–55.

[36] H.M. Soliman, Correlation of mist-to-annular transition during condensation, Can. J. Chem. Eng. 61 (1983) 178–182.

[37] J.A. Shmerler, I. Mudawar, Local heat transfer coefficient in wavy free-falling turbulent liquid films undergoing uniform sensible heating, Int. J. Heat Mass Transfer 31 (1988) 67–77.

[38] J.A. Shmerler, I. Mudawar, Local evaporative heat transfer coefficient in turbulent free-falling liquid films, Int. J. Heat Mass Transfer 31 (1988) 731–742.

[39] T.H. Lyu, I. Mudawar, Statistical investigation of the relationship between interfacial waviness and sensible heat transfer to a falling liquid film, Int. J. Heat Mass Transfer 34 (1991) 1451–1464.

[40] T.H. Lyu, I. Mudawar, Determination of wave-induced fluctuations of wall temperature and convective heat transfer coefficient in the heating of a turbulent falling liquid film, Int. J. Heat Mass Transfer 34 (1991) 2521–2534.

[41] I. Mudawar, R.A. Houpt, Mass and momentum transport in smooth falling liquid films laminarized at relatively high Reynolds numbers, Int. J. Heat Mass Transfer 36 (1993) 3437–3448.

[42] I. Mudawar, R.A. Houpt, Measurement of mass and momentum transport in wavy-laminar falling liquid films, Int. J. Heat Mass Transfer 36 (1993) 4151–4162.

[43] W. Qu, I. Mudawar, S.-Y. Lee, S.T. Wereley, Experimental and computational investigation of flow development and pressure drop in a rectangular micro-channel, J. Electron. Packag. – Trans. ASME 128 (2006) 1–9.